

# The gMOSS: the galaxy survey and galaxy populations of the large homogeneous field

Grokhovskaya A.,<sup>1,2\*</sup> Dodonov S.N.,<sup>1,2</sup> Movsessian T.A.,<sup>3</sup> Kotov S.S.<sup>1,2</sup>

<sup>1</sup> Special Astrophysical Observatory, Russian Academy of Sciences, Nizhny Arkhyz 369167, Russia

<sup>2</sup> Institute of Applied Astronomy of the Russian Academy of Sciences, Kutuzov Quay 10, St. Petersburg, 191187, Russia

<sup>3</sup> Byurakan Astrophysical Observatory, 0213 Aragatzotn prov, Armenia

Accepted XXX. Received YYY; in original form ZZZ

## ABSTRACT

We present the gMOSS (Galaxies of Medium-band One-meter Schmidt telescope Survey) catalog of  $\sim 19,000$  galaxies in 20 filters (4 broadband SDSS and 16 medium-band filters). We observed  $2.386 \text{ deg}^2$  on the central part of the HS47.5-22 field with the 1-m Schmidt telescope of the Byurakan Astrophysical Observatory. gMOSS is a complete flux-limited sample of galaxies with threshold magnitude  $r \text{ SDSS} \leq 22.5 \text{ AB}$ . From photometric measurements with 16 medium-band filters and  $u \text{ SDSS}$ , we obtain spectral energy distributions for each object in the field, which are used for further analysis. Galaxy classification and photometric redshift estimation based on spectral template matching with ZEBRA software. The obtained redshift accuracy is  $\sigma_{\text{NMAD}} < 0.0043$ . Using the SED-fitting CIGALE code, we obtained the main properties of the stellar population of galaxies, such as rest-frame  $(u - r)_{\text{res}}$  colour, stellar mass, extinction, and mass-weighted age with a precision of  $0.16 \pm 0.07 \text{ mag}$ ,  $0.14 \pm 0.04 \text{ dex}$ ,  $0.27 \pm 0.1 \text{ mag}$ , and  $0.08 \pm 0.04 \text{ dex}$ , respectively. Using a dust-corrected colour-mass diagram, we divided the full sample into populations of red and blue galaxies, estimated the evolution of the fractions of the populations with a redshift, and considered the dependencies between stellar mass and age. Throughout cosmic time, red sequence galaxies remain older and more massive than blue cloud galaxies. The star formation history of a complete subsample of galaxies selected in the redshift range  $0.05 \leq z \leq 0.015$  with  $\langle \log M \rangle_{[\text{M}_\odot]} > 8.3$  shows an increase in the star formation rate density up to  $z \sim 3$ , in accordance with the results obtained in earlier studies.

**Key words:** Astronomical data bases: surveys - cosmology: observations - galaxies: photometry – galaxies: evolution – galaxies: formation

## 1 INTRODUCTION

The evolution and physical properties of galaxies require statistical studies with a large number of objects. The use of spectroscopic redshifts is most preferable for analyzing the evolution physical properties of galaxies with the redshift. Spectroscopic redshifts were widely used in research on relatively bright galaxies with small redshift (e.g. in Peng et al., 2010). However, for samples of tens and hundreds of thousands of galaxies with high redshifts, fainter than  $I_{\text{AB}} = 22.0 \text{ mag}$  and without strong emission lines, this is practically impossible. Spectroscopy of such faint galaxies requires the largest telescopes and exposure times of several hours (Le Fèvre et al. 2005; Gerke et al. 2005; Meneux et al. 2006; Cooper et al. 2006; Coil et al. 2007; Lilly et al. 2007).

There are several medium-band surveys of sufficient depth that allow us to solve statistical problems of studying the physical properties of galaxies: COMBO-17 (Classifying Objects by Medium-Band Observations, a spectrophotometric 17-filter survey, Wolf et al. 2004), ALHAMBRA (Advanced Large, Homogeneous Area Medium Band Redshift Astronomical Survey, Moles et al. 2008), COSMOS (Cosmic Evolution Survey, Murayama et al. 2007), miniJPASS (a set of

J-PAS-like data for studies the scientific capabilities of J-PAS (The Javalambre–Physics of the Accelerating Universe Astrophysical Survey Benítez et al. 2009; Benítez et al. 2014), González Delgado et al., 2021). Some of these surveys were performed on small-sized areas that are significantly spaced apart, which makes it difficult to study the physical properties of galaxies depending on the density of the environment (e.g. COMBO-17, ALHAMBRA). Broadband surveys, due to the low accuracy of determining photometric redshifts and spectral type classification of galaxies, are excluded from consideration. Spectral surveys of sufficient area, such as SDSS (Sloan Digital Sky Survey, Peng et al. 2010) and 2dFGRS (The 2dF Galaxy Redshift Survey, Colless et al. 2003), are limited in-depth, while deep spectral surveys are insufficient in the area and samples are not complete due to the need for preliminary selection of objects. These are the reasons why photometric surveys using medium-band filters are becoming increasingly relevant.

In 2013 – 2015 the Laboratory of spectroscopy and photometry of extragalactic objects of the Special Astrophysical Observatory together with Armenian specialists upgraded the 1-m Schmidt telescope of the Byurakan Astrophysical Observatory of the National Academy of Sciences of Armenia (Dodonov et al. 2017). We completely redesigned the control system of the telescope: we replaced the actuating mechanisms, developed telescope control software, and

\* E-mail: grokhovskaya.a@gmail.com

made the guiding system. We redesigned and prepared a 4k x 4k Apogee (USA) liquid-cooled CCD with RON  $\sim 11.1$  e $^-$ , a pixel size of 0.868, and field of view of about 1 deg $^2$ , and in October 2015 mounted it in the focus of the telescope. The detector is equipped with a turret bearing 20 medium-band filters (FWHM = 250 Å) uniformly covering the 4000 — 9000 Å wavelength range, five broadband filters ( $u, g, r, i, z$  SDSS), and three narrow-band filters (5000 Å, 6560 Å and 6760 Å, FWHM = 100 Å). The main programs of the telescope are the search for young stellar objects, the evolution of AGN, the stellar composition of galaxy disks, and the study of the evolution of the main characteristics of galaxies.

The progress in the modern physics of galaxies, associated with the growth of the number of observational data and the development of numerical modeling methods, has not yet completely clarified the issues of the formation and evolution of galaxies. They still remain open and relevant. The variety of shapes and types of galaxies indicates that they evolve under the influence of a significant number of conditions: the density of the environment, the rate of accretion of external matter, internal secular evolution, the active nuclei feedback, etc. Each of these conditions affects the rate of star formation in the galaxy, which leaves an "imprint" on the history of star formation (SFH).

This work presents two parts of the gMOSS (Galaxies of Medium-band One-meter Schmidt Survey) photometric catalogue of 19,875 galaxies in a fixed aperture and 19,029 in a Kron-like apertures, high-precision photometric redshifts from 1-m Schmidt telescope of Byurakan Astrophysical Observatory and spectral observation on the 6-meter BTA telescope of SAO RAS. Section 2 briefly describes the data and observations. Photometry, redshift estimation and observational properties of the sample are given in Section 3. Section 4 consist of cluster galaxies catalogues descriptions. The process of estimating the physical parameters of galaxies and brief analysis of galaxy stellar population are described in Section 5. And we discuss our results in Section 6.

The paper uses the cold dark matter cosmological  $\Lambda$ CDM model with parameters  $\Omega_M = 0.315$ ,  $\Omega_\Lambda = 0.685$  and  $H_0 = 67.4$  km s $^{-1}$  (Planck Collaboration et al. 2018). All the stellar masses in this work are quoted in solar mass units ( $M_\odot$ ) and are scaled according to a universal Chabrier (2003) initial stellar mass function. All the magnitudes are in the AB system (Oke & Gunn 1983).

## 2 DATA AND OBSERVATIONS

In this work, we use the observational data of HS47.5-22 field (Hamburg Quasar Survey, Molthagen et al. 1997) obtained by the 1-meter Schmidt telescope (Dodonov et al. 2017) of the NAS RA Byurakan Astrophysical Observatory during several sets in February, March, April, and November of 2017 and in February and November of 2018 years. Telescope field of view with  $4\text{k} \times 4\text{k}$  CCD is  $58 \times 58$  arcmin, scale 0.868 arcsec pixel $^{-1}$ . Observations were made in 4 broadband filters ( $u, g, r, i$  SDSS) and 16 medium-band filters (FWHM = 250 Å with homogeneous coverage of the spectral range 4000 — 8000 Å). Medium-band with  $u$  SDSS filters are presented in Fig. 1.

The central part of the field was covered by four sets of exposures in broadband and medium-band filters. The overlap of adjacent sets was about 10 arcmin. The total exposure time was selected so as to reach a depth of  $m_{AB} \approx 25$  mag with a signal-to-noise ratio of  $\sim 5$  in broadband ( $\sim 2$  h) and  $m_{AB} \approx 23$  mag with a signal-to-noise ratio of  $\sim 5$  in medium-band filters (about 60 min at the peak of the detector sensitivity curve and about 2 h at the edges of the range). From these

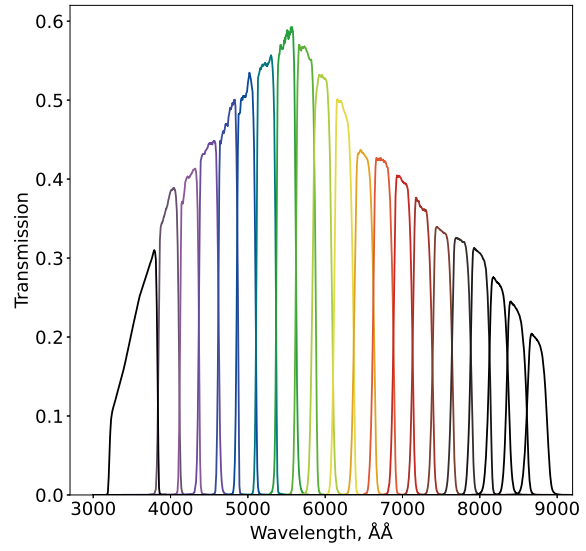


**Figure 1.** Set of 17 filters used for SED (Spectral Energy Distribution) construction. The leftmost passband corresponds to  $u$  SDSS filter and the others are medium-band filters. Filter transmission was measured in F/2, the spectral sensitivity of the CCD detector were taken in account.

observations, we create a mosaic of  $4 \times 1$  deg $^2$  fields with total area of 2.386 deg $^2$ .

In addition, we carried out long-slit spectral observations of certain galaxies with the Russian 6-m telescope with SCORPIO-2 multimode reducer of the telescope prime focus (Afanasiev & Moiseev 2011). The observations took place on 25, 28 of February 2020 (under the seeing 2.1 and 3.0 arcsec respectively) and 13, 14 of December 2020 (under the seeing 1.5 and 1.3 arcsec respectively). The slit width was 2 arcsec. We used the grism VPHG940@600, which covers the spectral range 3500 — 8500 Å and has a dispersion of 1.16 Å pixel $^{-1}$ . The spectral resolution is  $\sim 7.0$  Å ( $R \sim 5200$ ) estimated as FWHM for 1 arcsec slit of night-sky emission lines. The total exposure time was selected so as to get a signal-to-noise ratio of  $\sim 5 - 10$ .

We processed the spectra of all objects that hit the slit and had a sufficient signal-to-noise ratio. We obtained the spectra of 29 galaxies. We used a standard processing software package for spectra obtained by multimode focal reducer SCORPIO-2. The data reduction steps include bias subtraction, cosmic particle removing, flat-field correction, wavelength calibration, sky subtraction, correction for the atmospheric and spectrograph transparency by spectrophotometric standards, and extraction to 1D spectrum. The accuracy of the spectral redshift estimation for all galaxies is 0.002.

All data is available to the reviewer(s) on <https://github.com/alegro/gMOSS> and will be made open-source on publication.

Also, we use spectral and photometric data from the SDSS database (Sloan Digital Sky Surveys, Data Release 16, Ahumada et al. (2020)) for calibration photometric redshifts and GAIA DR2 Gaia Collaboration et al. (2016, 2018) to exclude objects with proper motions (like stars).

### 3 OBSERVATION DATA ANALYSIS

This section presents a brief summary of the observation data analysis methods used in the gMOSS survey.

#### 3.1 Photometry

Photometry of the objects was obtained using SExtractor (Bertin & Arnouts 1996) in dual image mode. The base image was created from the sum of deep ( $\sim 25$  mag) images obtained in  $g$ ,  $r$  and  $i$  SDSS filters. Before the photometry, all images were convolved to common seeing quality and transformed to a common coordinate system. For galaxy type classification and redshift estimation, we use photometry in fixed apertures MAG\_APER and correct received fluxes for light loss using a light curve obtained from bright stars. The diameter of the aperture was 3 arcsec. Using a fixed aperture allows us to reduce the number of objects with strongly biased aperture photometry by neighboring sources. For galaxy physical parameter estimation we received Kron-like fluxes for 97 per cent galaxies of the total sample in the field by using MAG\_AUTO SExtractor photometry because of large photometric errors for some faint sources. Photometric calibration was developed using spectral and photometric data from the SDSS survey for the objects detected in the field. By using field objects as standard stars within each exposure, we were independent of photometric conditions during imaging.

The galaxy sample of the HS47.5-22 field is limited by the threshold magnitude  $m_{AB} = 22.5$  mag in the  $r$  SDSS filter with redshift  $z \leq 0.8$ . The total number of field objects down to  $m_{AB} \sim 25$  mag is approximately 85,000; the sample of galaxies intended for the study included 18,079 galaxies with photometric data in a fixed aperture and 17,545 galaxies with the use of Kron-like apertures applicable to the selection criteria (see Section 3.3).

Photometric measurements from 17 filters provide low-resolution spectra for each object which are analyzed by a statistical technique for classification and redshift estimation based on spectral template matching. SEDs for 4 galaxies from HS47.5 - 22 field in 16 medium-band filters and their SDSS spectra are shown in Fig. 2. The main spectral features such as H+K Ca II, Mg, H  $\alpha$ , [O II], [O III] and others are clearly visible in the SEDs. The photometric properties of a galaxy sample of the HS 47.5-22 field were investigated in the range of 4000 Å up to 8000 Å, which allows you to confidently determine the redshifts of galaxies from  $z = 0$  to  $z = 0.8$ .

#### 3.2 Photometric redshifts

The method for determining the photometric redshift and SED type of a galaxy is based on the correspondence of the spectral templates of the galaxy to the observed energy distribution. We used the galaxy's spectral templates library from Dodonov & Chilingarian (2008), and a set of programs ZEBRA (Zurich's Extragalactic Bayesian Redshift Analyzer, Feldmann et al. 2006).

The obtained redshift accuracy is  $\sigma_{\text{NMAD}} < 0.0043$  and the fraction of catastrophic outliers is  $(\Delta z/(1+z) > 5 \cdot \sigma_{\text{NMAD}}) \sim 7.7$  per cent. Figure 3 shows a comparison of the photometric redshifts of galaxies obtained using the ZEBRA software tool and the spectroscopic redshifts from the SDSS database. The total number of galaxies with spectroscopic redshifts in the observed HS47.5-22 field is 414. Accuracy  $\sigma_{\text{NMAD}}$  changes from 0.002 for objects brighter than 19.0 mag in  $r$  SDSS filter and 0.006 for objects brighter than 21.0 mag till 0.007 for objects brighter than 22.5 mag.

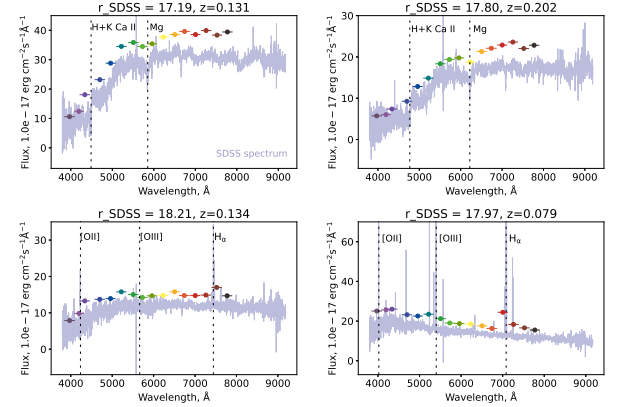


**Figure 2.** SED for 4 galaxies from HS47.5-22 field. The horizontal bar is the filter bandwidth, and the solid line is the spectra of these objects from the SDSS survey. Flux differences seen on the picture are due to the limited size of the fibers (3 arcsec) used for spectroscopy. The main spectral features (e.g. H+K Ca II, Mg, H  $\alpha$ , [O II] and [O III] - dashed lines) of each object are also clearly visible in the SEDs.

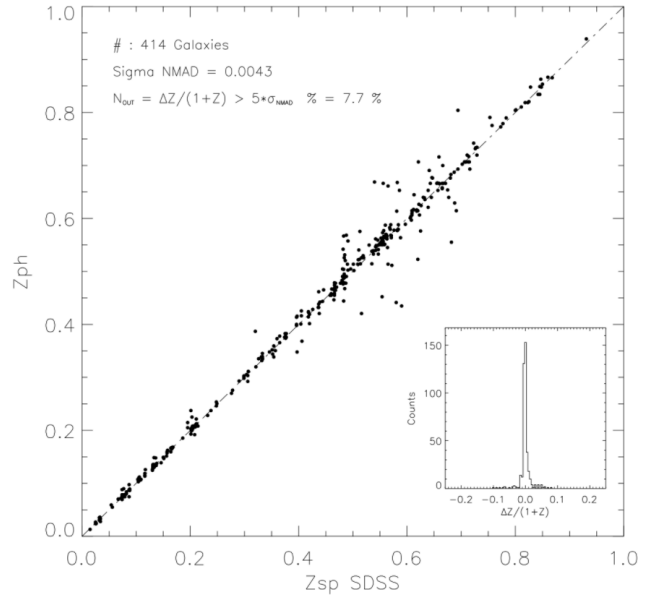


**Figure 3.** Comparison of the photometric redshifts  $z_{\text{ph}}$  of the galaxies obtained with the ZEBRA software tool with the spectroscopic redshifts  $z_{\text{sp}}$  of the galaxies taken from SDSS for 414 galaxies with spectroscopy. The accuracy of determining the photometric redshift is  $\sigma_{\text{NMAD}} < 0.0043$ , the outlier's percentage is  $\Delta z/(1+z) > 5 \cdot \sigma_{\text{NMAD}} \sim 7.7$  per cent. Accuracy  $\sigma_{\text{NMAD}}$  changes from 0.002 for objects brighter than 19 mag in  $r$  SDSS filter and 0.006 for objects brighter than 21 mag till 0.007 for objects brighter than 22.5 mag. The dashed line denotes a line of equal photometric and spectral redshifts.

### 3.3 Galaxy sample

A sample of galaxies for the study was made from a complete photometric survey (approximately 85,000 objects down to  $m_{AB} \sim 25$  mag) according to the following criteria:

- (i) To exclude objects with proper motions, such as stars, we used data from the GAIA DR2 survey (Gaia Collaboration et al. 2016, 2018);
- (ii) To exclude stars (without proper motions in the GAIA survey), we remove objects for which the morphological classification from the DECATS survey (Dey et al. 2019) is STAR;
- (iii) To exclude objects with strongly biased aperture photometry by neighboring sources or by a large number of bad pixels in any aperture we include to the sample only objects with the automatic index of contamination of SExtractor, as provided by the FLAGS  $\leq 2$ ;
- (iv) To define a flux-limited sample, we imposed the condition that the galaxies have to be brighter than  $r_{AB} = 22.5$  mag;

Applying this set of criteria to the initial sample of more than 85,000 objects, we obtained a sample of galaxies, selected according to  $r$  SDSS magnitude, extended and contamination index. Our final sample of objects with aperture photometry contains 19,875 extended and non-contaminated sources with  $r_{AB} \leq 22.5$ . For Kron-like photometry, we obtain 19,029 objects because of large photometric errors for some faint sources. MAG\_AUTO provides the total flux of source within an elliptical aperture determined by the KRON\_RADIUS, MAG\_APER measure for a smaller fixed aperture (3 arcsec).

It should be noted that the final gMOSS survey contains galaxies with a wide variety of spectrum types, colours, and environments (see Fig. 2 and Grokhovskaya et.al., 2022, in prep.). The SEDs of galaxies on upper panels of Fig. 2 shows the power of gMOSS to identify red galaxies, to detect the absorption lines such as H+K Ca II and Mg. Blue and star-forming galaxies with the recombination nebular lines H  $\alpha$  and the other nebular collisional lines, such as [O II]  $\lambda\lambda 3727$  and [O III]  $\lambda\lambda 5007$  are also very well-identified in the survey (see the bottom panel in Fig. 2). Galaxies in groups, as well as galaxies in less dense environments, are well identified because we use a fixed 3 arcsec aperture to identify objects. It allows us to analyze the dependence of the physical properties of galaxies on the density of environments in the next work.

The completeness of the sample of galaxies number-counts in  $g$ ,  $r$  and  $i$  SDSS filters was verified by comparison with previously published data in the papers Yasuda et al. (2001); Capak et al. (2004); Kashikawa et al. (2004). Results are shown in Fig. 4. The galaxy sample is complete up to  $m_{AB} = 23.0$  mag with no colour selection effects in the all-optical range.

### 3.4 Observational properties of sample

Figure 5 compares the distributions of redshift, magnitude and error in the  $r$  SDSS band of the full sample of gMOSS galaxies and the final selected sample of galaxies up to  $z = 0.8$ . As can be seen from the top-right panel of Fig. 5, the redshift sampling limit excludes most of the galaxies with significant errors in determining the magnitude in the  $r$  SDSS filter, as well as some of the faint objects in the sample. After the redshift  $z = 0.3$ , we observe a sharp increase in the number of objects associated with a rapid increase in the observed volume. After the redshift  $z = 0.6$ , there is a decrease in the number of objects because of the selected threshold on the magnitude  $r_{AB} \leq 22.5$ . Most

of the galaxies in the sample have a photometric redshift between 0.2 and 0.6.

Figure 6 shows the correlation between the magnitude of objects in the  $r$  SDSS filter and photometry errors, both in the  $r$  SDSS filter and for the average error in the medium-band filters. For photometry in Kron-like apertures, we obtained a strong increase in the average error in the medium-band filters for faint objects. This is due to the fact that faint objects ( $r$  SDSS  $\sim 20.5$  mag) in the part of the medium-band filters have an insufficient signal-to-noise ratio ( $S/N \leq 5$ ) for the correct operation of the photometry algorithm with Kron-like apertures. The *bottom left panel* shows galaxies with a Kron-like aperture, which are used to obtain the properties of stellar populations of galaxies using the SED-fitting code CIGALE (Burgarella et al. 2005; Noll et al. 2009; Boquien et al. 2019). The conditions for using the data in the Kron-like apertures were that the median error of the photometry was less than 1 mag and at least half of the filters were with a sufficient signal-to-noise ratio ( $S/N \geq 5$ ) for detecting an object by the Kron-like aperture detection algorithm. Thus, we were able to use Kron-like photometry data for 9620 galaxies from a complete sample. For the rest of the galaxies, we used aperture photometry data. This is true for estimating distant faint objects whose dimensions do not exceed 3 arcsec.

The magnitude in the  $r$  SDSS band shows a dependence on redshift Fig. 7. Galaxies with  $r$  SDSS  $\leq 20.0$  mag (fixed aperture photometry) are often located at  $z < 0.5$ , while fainter galaxies are at any distance. The S/N ratio is also a clear function of the brightness of the galaxy, as indicated by the magnitude in the  $r$  SDSS filter and median S/N ratio in the medium-band filters. The increase in the S/N for Kron-like aperture photometry with respect to fixed aperture photometry is clear in Fig. 7, although this increase is quite significant. For instance, galaxies with  $r$  SDSS  $\sim 21.0$  mag have an  $S/N \sim 10$  for fixed aperture apertures, while for Kron-like apertures this value is  $\sim 3$ . Therefore, for galaxies with an insufficient signal-to-noise ratio for Kron-like photometry ( $S/N \leq 5$ , typically these are galaxies fainter than 20.5 mag in  $r$  SDSS filter), we use fixed-aperture photometry data for analysis of galaxy physical properties.

We can fit  $\sim 74$  per cent of the full gMOSS galaxy survey (in a combination aperture photometry and Kron-like photometry data) with the CIGALE (Burgarella et al. 2005; Noll et al. 2009; Boquien et al. 2019) SED-fitting code with an acceptable parameter value of reduced  $\chi^2$  (see Section 5). The unfitted spectra do not fulfill quality requirements imposed by the SED-fitting codes, such as the minimum S/N in each band. We select the total exposure time so as to obtain a signal-to-noise ratio of  $\sim 5 - 10$  for objects brighter than  $r$  SDSS = 22.5, however, for some faint objects this time may not be sufficient to achieve the required S/N ratio.

## 4 CATALOGUE DESCRIPTION

We prepare two catalogues that were used for the analysis of stellar populations and photometric redshifts of galaxies: photometry of galaxies in fixed apertures (aperture size 3 arcsec) and Kron-like apertures as two parts of gMOSS galaxy catalogue. Both catalogues have the same structure as shown in the Table ???. The columns of the table contain the following information about the catalogue: (1) - parameter name, (2) - unit of parameter (3) - description of parameter. The magnitudes are in the AB magnitude system and are not corrected for Galactic extinction.

Catalogues include unique object IDs, R.A. and Dec. coordinates (J2000), photometric measurements in 16 medium-band and 4 broad-band SDSS filters, and their errors for each object and the accurate

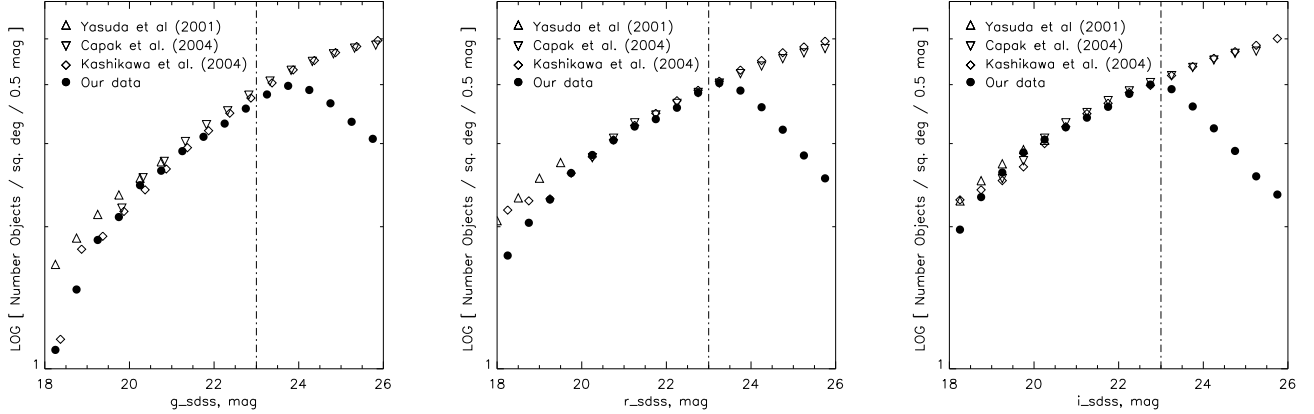


**Figure 4.** Comparison of the completeness of the galaxy sampling in the  $g$ ,  $r$ , and  $i$  SDSS filters in the previously published data and the data obtained in this work. The figure shows the lack of colour selection effects down to  $m_{AB} = 23$  mag.

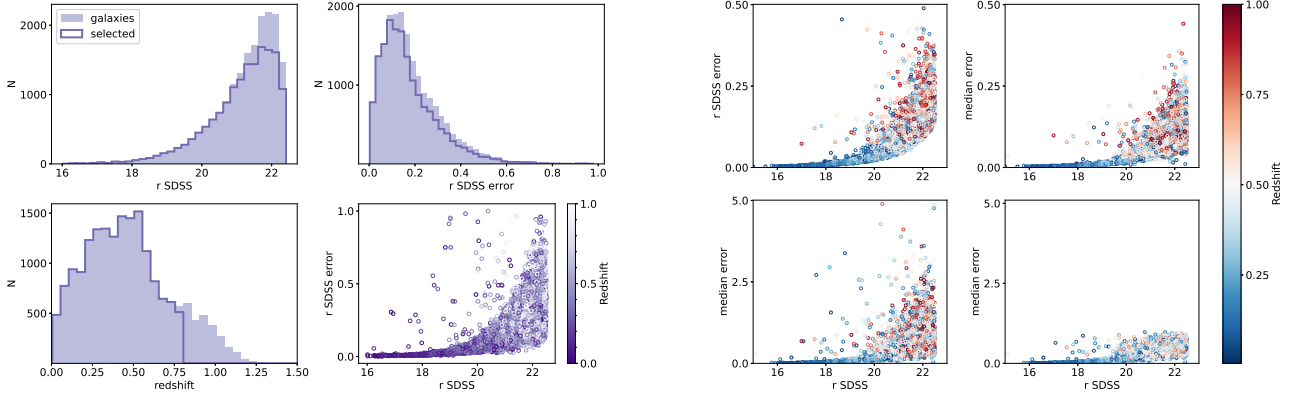


**Figure 5.** Distributions of several observational properties. *Top-left, top-right and bottom-left panels:* Distribution of  $r$  SDSS magnitude and errors, and redshifts of galaxies with  $r$  SDSS  $\leq 22.5$  mag identified in gMOSS (light purple) and galaxies with  $z \leq 0.8$  (dark purple) and photometric redshifts  $z \leq 0.8$ . All magnitudes and related errors were obtained using SExtractor. *Bottom-right:* Errors of the  $r$  SDSS as function of  $r$  SDSS band magnitude. The colour bar illustrates the redshift of each galaxy.

photometric redshifts ( $\sigma_{\text{NMAD}} < 0.0043$  for all types of galaxies in full magnitude range) obtained from fixed aperture photometry data with spectral template matching by using a set of programs ZEBRA (Feldmann et al. 2006). The unique object ID is a combination of the field number in the mosaic and the unique object number in each field (NB: the numbers of objects in different fields may overlap, so we additionally use the field identifier). In addition, we included data on spectroscopic redshifts from the SDSS survey for those galaxies for which this was possible (Ahumada et al. 2020) and data on spectroscopic redshifts of 29 galaxies obtained with a 6-meter Russian telescope. The catalogues contain galaxies brighter than 22.5 mag in  $r$  SDSS filter.

The total number of galaxies in the catalogue with photometric data in a fixed aperture is 18,079 galaxies, with the use of Kron-like apertures - 17,545. The number of objects in the catalogue with Kron-like apertures is slightly less than the number of objects in the

**Figure 6.** Errors of the  $r$  SDSS band (*Top left panel*) and medium-band filters (*Top right panel*) as a function of the  $r$  SDSS magnitude. The *top panels* show the aperture photometry. The *bottom panels* show the Kron-like photometry and errors of the medium-band photometry. *Bottom left panel:* full sample of galaxies, *Bottom right panel:* part of the complete sample, which is used to analyze the properties of the stellar population of galaxies. The colour bar illustrates the redshift of each galaxy.

catalogue with a fixed aperture due to the fact that this method does not separate close objects well.

..

In addition, in a separate table we publish galaxies with spectral redshifts which were obtained with the Russian 6-meter telescope BTA and SCORPIO-2 multi-mode focus reducer. The columns of the table contain the following information about observations: (1) - unique galaxy id, (2), (3) - coordinates RA and DEC in degrees, (4) - spectroscopic redshift, (5) - exposition of observation.

All data is available to the reviewer(s) on <https://github.com/alegro/gMOSS> and will be made open-source on publication.

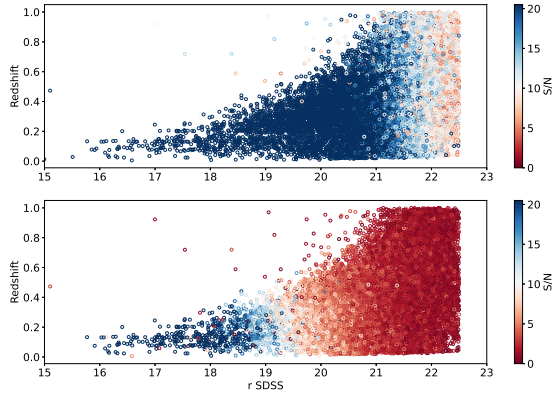


**Figure 7.** Galaxy observed magnitudes in the  $r$  SDSS filter as a function of redshift for fixed aperture and Kron-like photometry (*Top* and *bottom* panels, respectively). The colour bar shows the median S/N ratio in the medium-band filters.

## 5 STELLAR POPULATION PROPERTIES OF GALAXIES IN THE SAMPLE

This section describes the distributions of the stellar population properties obtained with CIGALE SED-fitting code for the Kron-like MAG\_AUTO photometry of gMOSS catalogue.

To analyze the physical properties of stellar populations of galaxies, we used only objects up to  $z \sim 0.8$ , since most of the extended objects at  $z \geq 0.8$  are fainter than 22.5 mag and are barely detected, and we do not have a sufficient number of objects for statistical analysis. The total number of galaxies for stellar populations properties estimation is 16,509.

### 5.1 SED-fitting code parameters

There are many modern codes for SED-fitting spectra in the full spectrum range from X-rays to radio such as ProSpect (Robotham et al. 2020), BEAGLE (Chevallard & Charlot 2016), BAGPIPES (Carnall et al. 2018), CIGALE (Burgarella et al. 2005; Noll et al. 2009; Boquien et al. 2019), Prospector (Leja et al. 2017; Johnson et al. 2020), MAGPHYS (da Cunha et al. 2008), BaySED (Han & Han 2012, 2014, 2019) and others. The stellar mass, rest frame colours, ages and other physical parameters in this work are derived using the CIGALE code. CIGALE (Code Investigating GALaxy Emission) is a multi-wavelength spectral energy distribution (SED) fitting code for extragalactic studies. The code has been developed to study the evolution of galaxies by comparing modeled galaxy SEDs to observed ones from the far X-rays to the radio.

Through template fitting, a series of stellar population parameters can be obtained, such as the rest frame  $(u - r)_{\text{res}}$  colour, the mass-weighted age, V-band attenuation  $A_v$ , total stellar mass, age of the main stellar population in the galaxy, metallicity, and star formation rate. Modelling the stellar component of galaxies is done by the default BC03 (Bruzual & Charlot 2003) spectral evolution synthesis models with the Chabrier (2003) initial mass function. We considered a set of six discrete metallicities: 0.0001, 0.0004, 0.004, 0.008, 0.02, 0.05. A delayed SFH with optional exponential burst and thirteen different values of star formation timescale ranging from 1 to 12 Gyr is assumed. The modified Calzetti et al. (2000) attenuation law

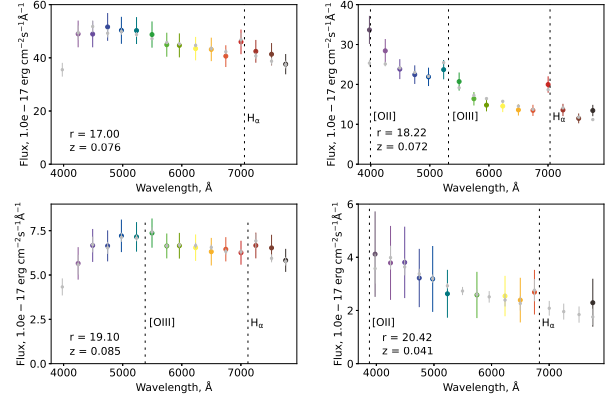


**Figure 8.** MAG\_AUTO SEDs for different galaxies with brightness  $17.0 \leq r_{\text{SDSS}} \leq 20.42$  mag in the redshift range  $z = 0.04 - 0.08$  are shown by colour dots. The colour bars around these dots show the  $\pm 1\sigma$  variation. The Bayes model fitted to the spectral energy distribution with CIGALE is plotted as gray dots, and the gray bars show the magnitudes of the mean model at the  $\pm 1\sigma$  uncertainty level.

is used with a ratio of total to selective extinction for the extinction curve applied to emission lines  $r_V = 3.1$  (the average value for the Milky Way). Dust emission model (Draine et al. 2014), nebular and rest-frame parameters modules are also used.

### 5.2 Fitting and quality assessment

SED-fitting reproduces well enough the values in 16 medium-band and  $u$  SDSS filters of various types of galaxies in gMOSS sample within uncertainty and regardless of the redshift and brightness range. Figure 8 shows nearby galaxies (up to  $z = 0.1$ ) in the magnitude range from 18.0 to 21.0 mag in  $r$  SDSS filter. The main spectral features of early (e.g. H+K Ca II, Mg) and late-type galaxies (e.g. H  $\alpha$ , [O II] and [O III]) are also well reproduced. SED-fitting uncertainties increase towards the fainter magnitudes because of the higher uncertainties in the data, which also increases for fainter objects.

The spectral energy distributions from the gMOSS catalogues are well reproduced by the SED-fitting code CIGALE. The quality of the correspondence for the entire sample of galaxies can be estimated using the reduced  $\chi^2$ -parameter. The dependence of the  $\chi^2_{\text{reduced}}$  parameter on the signal-to-noise ratio is shown in Figure 9, the colour bar corresponds to the redshift for each object. The discretization of the signal-to-noise ratio distribution for bright galaxies is due to the limitation of photometry accuracy. As expected, there is some inverse dependence for the chi-squared parameter value on the signal-to-noise ratio:  $\chi^2_{\text{reduced}}$  parameter estimates are minimal for bright objects, while with a decrease in the signal-to-noise ratio, the SED-fitting of objects becomes less accurate. The  $\chi^2_{\text{reduced}}$  parameter increases with a decrease in the signal-to-noise ratio and an increase in the redshift value. About half of the objects have  $\chi^2_{\text{reduced}} \leq 0.5$ , and for  $\sim 60$  per cent of objects,  $\chi^2_{\text{reduced}} \leq 1.5$ . We obtained rather small values for the reduced  $\chi^2$  parameter, which indicates a quite well accuracy in estimating the physical quantities of the galaxies in the sample.

We can fit 12,281 galaxies of the 16,509 objects from the full sample ( $\sim 74$  per cent) with the CIGALE SED-fitting code. This number

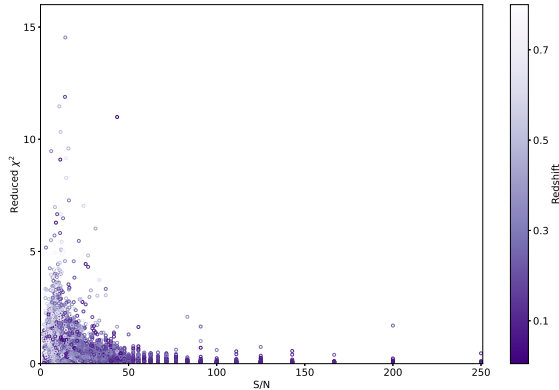


**Figure 9.** Distribution of reduced  $\chi^2$  parameter and signal-to-noise ratio (S/N) in  $r$  SDSS filter for objects with MAG\_AUTO photometry. Colour bar indicates the redshift of each galaxy. The discretization of the signal-to-noise ratio distribution for bright galaxies is due to the limitation of photometric accuracy.

of objects is sufficient to study the statistical dependencies of the physical properties of galaxies in the entire studied redshift range  $0 < z \leq 0.8$ .

### 5.3 Distributions of stellar population properties

Fig. ?? shows distributions of selected physical properties of fitted galaxies. The purple gradient lines show the quality of SED-fitting (reduced  $\chi^2$ -parameter). The colour  $(u - r)_{\text{res}}$  shows the bimodal distribution of galaxies, where the maximum density is at  $(u - r)_{\text{res}} \sim 1.5$  mag for blue galaxies and  $(u - r)_{\text{res}} \sim 2.5$  mag for the red sequence. The bimodal distribution becomes more clear for objects with a decrease in the value of the  $\chi^2_{\text{reduced}}$  parameter. The mass-weighted age distribution  $\langle \log \text{age} \rangle_M [\text{yr}]$  has two peaks on  $\sim 9.0$  and  $\sim 9.6$  dex.

The extinction  $A_V$  for the sample of galaxies is distributed in the range from 0 to 1.4 mag, which is slightly less than the ranges obtained in other works (for example, in the González Delgado et al. 2021, the extinction is in the range from 0 to 2.0 mag). This is due to the choice of the observation field, which is located in an area with a very low density of neutral hydrogen on the visual beam  $\langle N_H \rangle = 10^{20} \text{ cm}^{-2}$ , which is not much higher than the absorption value in the "Lockman Hole" region (Lockman et al. 1986), where the lowest absorption on the visual beam is observed for the northern sky  $\langle N_H \rangle = 4.5 \cdot 10^{19} \text{ cm}^{-2}$ .

The stellar mass distribution ranges from  $\sim 7$  to  $\sim 11.5$  dex. The age of the main stellar population distribution  $\langle \log \text{age} \rangle [\text{yr}]$  has two peaks on  $\sim 9.4$  and  $\sim 9.9$  dex. Metallicity is distributed discretely due to the initial conditions for calculating models.

### 5.4 Mass–colour diagram

To study the differences between the red and blue populations of galaxies, it is customary to use mass-colour diagrams (Díaz-García et al. 2019; Schawinski et al. 2014; Moresco et al. 2013). The rest-frame colour  $(u - r)_{\text{res}}$  shows that the galaxies are quite clearly divided into these two populations. Fig. 10 shows the mass-colour

diagrams in combination with the parameters of the mass-weighted age, metallicity and extinction. The mass-colour diagram with the mass-weighted age parameter (Fig. 10, left) shows the apparent separation of galaxies into younger blue galaxies with  $\log(\text{age})_M [\text{yr}]$  down to  $\sim 9.4$  dex and older red ones with  $\log(\text{age})_M [\text{yr}]$  above  $\sim 9.5$  dex. Most galaxies have solar metallicity, however, super-solar values are often found for red sequence galaxies and low-metallicity values for blue galaxies. The extinction value practically does not depend on which population of galaxies it is determined for. However, it is worth noting that  $A_V > 1.0$  mag is typical for galaxies with  $(u - r)_{\text{res}} \sim 1.5$  mag, which roughly corresponds to the galaxies from the green valley. This fact is consistent with the assumption that the green valley galaxies are star-forming galaxies from the blue cloud (Díaz-García et al. 2019; González Delgado et al. 2021).

### 5.5 The accuracy of determining the properties of the stellar population

Uncertainties in determining the physical properties of galaxies were obtained within the SED-fitting process by the CIGALE code. Figure 12 shows the distribution of the accuracy of the physical properties of galaxies in the colour-mass diagram. The parameter of the age of the main stellar population of the galaxy has the best precision of estimation:  $\sigma(\log(\text{age})_L) = 0.05 \pm 0.04$  dex. Estimates of the accuracy of total stellar mass, the mass-weighted age and the rest frame  $(u - r)_{\text{res}}$  colour, are fairly well obtained:  $\sigma(\log(M) [M_\odot]) = 0.12 \pm 0.05$  dex,  $\sigma(\log(\text{age})_M) = 0.10 \pm 0.04$  dex and  $\sigma(u - r)_{\text{res}} = 0.19 \pm 0.08$  mag. The stellar extinction precision is  $\sigma(A_V) = 0.28 \pm 0.09$  mag. The accuracy depends on the signal-to-noise ratio and resolution in SEDs. The accuracy estimates obtained are quite similar to the accuracy estimates of physical parameters from other works, for example from (González Delgado et al. 2021). The average value of S/N in our sample is  $\sim 10$  but our resolution is more than two times worse than in miniJPAS survey (FWHM filters is 100 Å) thus, the accuracy of our estimates is somewhat lower.

The colour-mass diagrams in Figure 11 show that the value of errors in determining the physical parameters of galaxies is not the same for different populations of galaxies. The bimodality of the distribution is clearly visible in the diagrams showing the error of determining both the mass-weighted age and the age of the main stellar population. For red sequence galaxies, this value rarely exceeds ( $\sigma(\log(\text{age})_M) \leq 0.1$  dex and  $\sigma(\log(\text{age})_L) \leq 0.1$  dex). In addition, the mass of the main stellar population is also determined better for red galaxies  $\sigma(\log(M) [M_\odot]) \leq 0.1$  dex than for blue cloud galaxies and  $\sigma(u - r)_{\text{res}}$  is constrained slightly better in the red sequence than in the blue cloud. The uncertainties in  $A_V$  are the same for blue cloud galaxies, while a higher value of  $\sigma(A_V)$  corresponds to more massive galaxies in the red sequence.

## 6 DISCUSSION

The accuracy of the estimation of photometric redshifts in our sample of galaxies ( $\sigma_{\text{NMAD}} < 0.0043$ ) makes it possible to study the evolution of the physical properties of galaxies with cosmic time. Our survey is actually the largest in the area (the total homogeneous area is  $2.386 \text{ deg}^2$ ) among the mid-band deep surveys at the moment, which makes its data fairly homogeneous and complete. Sufficient SED resolution (FWHM of a medium-band filter is 250 Å) makes it possible to divide galaxies into a red sequence and a blue cloud and to study their properties independently of each other through cosmic time.

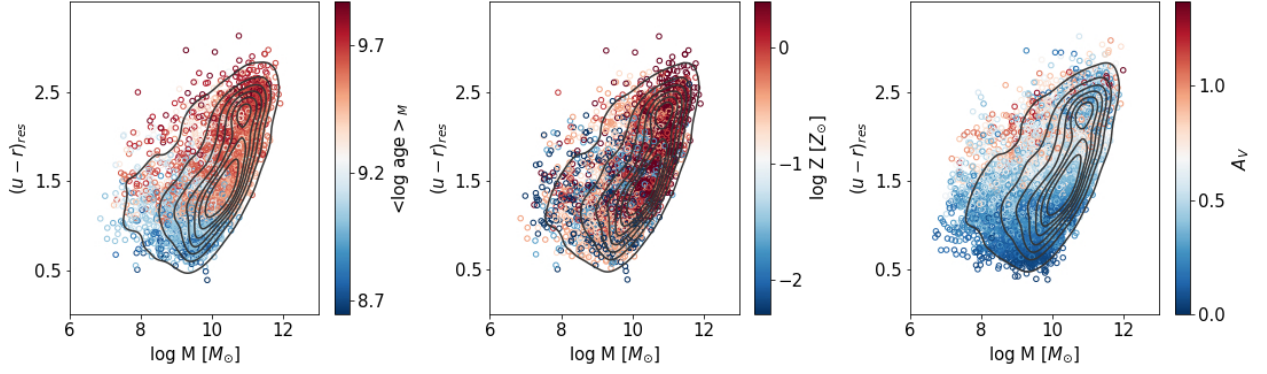


**Figure 10.** Mass–colour relation, with the coloured bar showing the stellar population properties of the galaxies: age, metallicity and extinction. Properties were derived using the MAG\_AUTO photometry.

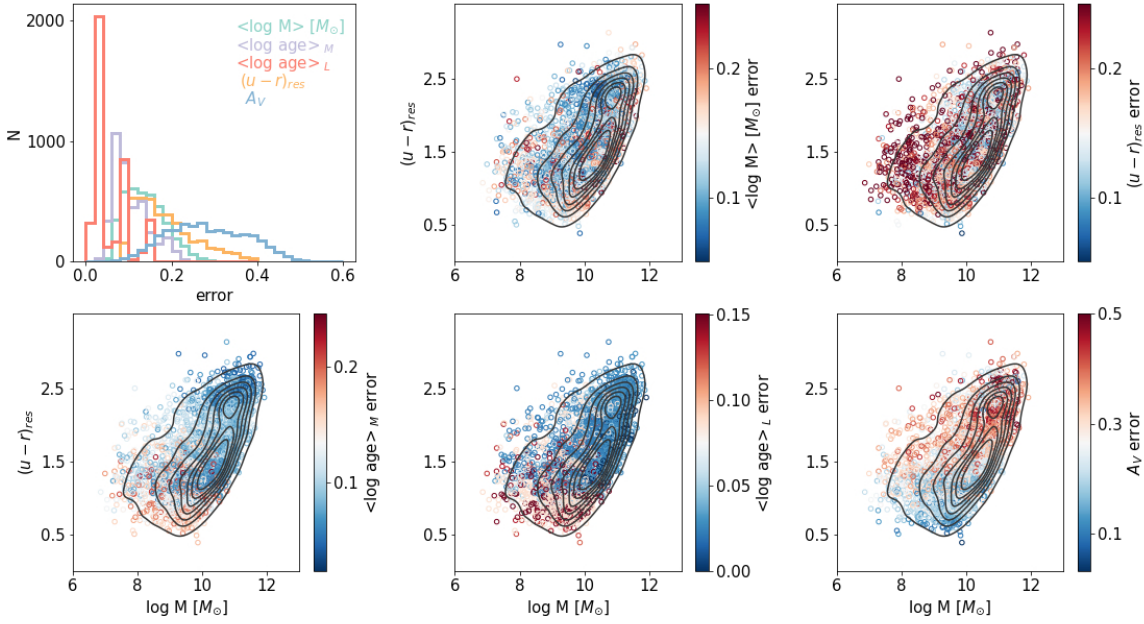


**Figure 11.** Distribution of standard deviations of galaxy properties (*top-left panel*) and the colour–mass plane coloured by the standard deviation of the stellar population properties: total stellar mass, the rest frame  $(u - r)_{\text{res}}$  colour, the mass–weighted age, age of the main stellar population in the galaxy and V-band attenuation  $A_V$ .

In our work, there was no goal of a detailed study of the evolution and formation of galaxies depending on the redshift. We investigated the physical properties of galaxies in general and compared the results obtained with previous works by other authors. For the correct interpretation of the results, it is necessary to take into account that there is a limit on the visibility of galaxies of a certain absolute galaxy magnitude at a certain redshift (Malmquist bias, [Malmquist 1922](#)). Thus, the least massive galaxies fall out of the field of our consideration with an increase in redshift. We leave the study of the bias to the region of more massive galaxies outside the scope of this

work. However, it should be noted that Figure 12 shows that galaxies with a mass less than  $10^8 M_\odot$  occur only at lower redshifts.

To analyze the general physical properties of galaxies, we planned to use photometry obtained in Kron-like apertures. However, in the course of the study, data were obtained that showed that Kron-like photometry is effective only for galaxies up to  $r_{AB} = 20.5$  mag, then the uncertainties associated with determining the Kron radius for objects begin to arise due to the insufficient signal-to-noise ratio. Therefore, for objects fainter than  $r_{AB} = 20.5$  mag, we used aperture photometry.

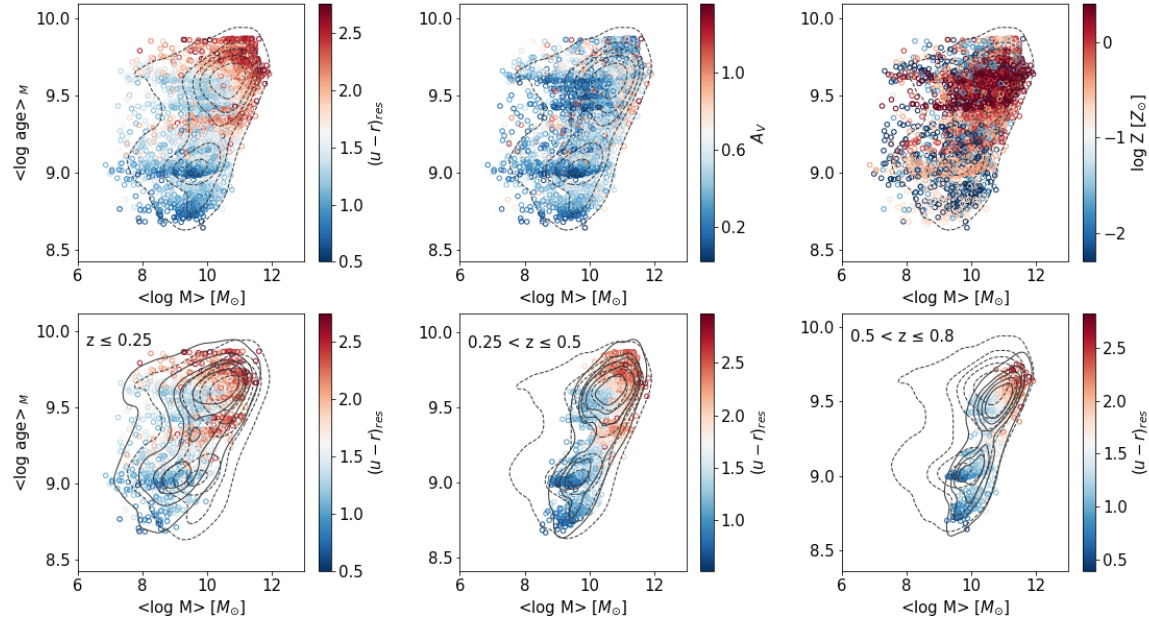


**Figure 12.** The top panel: Distributions of the rest frame  $(u - r)_{\text{res}}$  colour, V-band attenuation  $A_V$ , and metallicity across the mass–age relation. The values of all the parameters are coded according to the colour bars. The bottom panel illustrates the points and contour distribution of the rest frame  $(u - r)_{\text{res}}$  colour in the mass–age relation at  $z \leq 0.25$ ,  $0.25 < z \leq 0.5$ , and  $0.5 < z \leq 0.8$ . The dashed contours show the distribution of galaxies with  $z \leq 0.8$ . The discretization of the age values of galaxies occurs due to the limitations of computing power for the initial set of calculated values.

### 6.1 Evolution of galaxy populations in the mass - age diagram

Like the colour-mass diagram, the bimodality in the distribution of galaxies is quite clearly visible in the mass-age  $\log(M)_{[M_\odot]} - \log(\text{age})_M$  (Fig. 13). The oldest galaxies in the sample have redder colours, a larger mass and a higher metallicity value.

In recent works (Kauffmann et al. 2003; González Delgado et al. 2014, 2021), it is shown that bimodality is also observed in the fact that galaxies from the blue cloud have a linear dependence of age on the stellar mass of the galaxy. In our work, we also find this dependence (Fig. 12, bottom panels). This dependence is most clearly manifested if we analyze galaxies from the same cosmic epochs. For this purpose, we divided our sample into three bins:  $z \leq 0.25$ ,  $0.25 < z \leq 0.5$  and  $0.5 < z \leq 0.8$ . At a small redshift, the mass-age ratio shows a change in the slope of the dependence for galaxies with a mass greater than  $\log(M)_{[M_\odot]} = 10.5$  dex, for which the ratio  $\log(M)_{[M_\odot]} - \log(\text{age})_M$  is becoming quite slightly sloping in comparison with the late-type galaxies. This mass limit refers to the green valley galaxies, which are the transition from the blue cloud to the red sequence. Analyzing the red galaxies of all three bins by redshift, it is noticeable that with decreasing age, the mass of the galaxy also decreases. Thus, we can assume that the least massive galaxies formed in later cosmic epochs.

### 6.2 Evolution of galaxy populations in the mass - age diagram with extinction correction

Dust extinction reddens galaxies, so it is important to study the colour - mass ratio not only for the colour  $(u - r)_{\text{res}}$  in the rest system

but also for the colour  $(u - r)_{\text{int}}$  in the rest system corrected for extinction (so-called intrinsic colour). After extinction correction, the ratio between the galaxies of the red sequence and the blue cloud changes significantly (Schawinski et al. 2014; Díaz-García et al. 2019).

Figure 13 shows the distribution of galaxies in the colour-mass diagram for the rest frame colour  $(u - r)_{\text{res}}$  and for the intrinsic colour  $(u - r)_{\text{int}}$  in three redshift bins:  $z \leq 0.25$ ,  $0.25 < z \leq 0.5$ , and  $0.5 < z \leq 0.8$ . It can be seen that the distribution of galaxies in the colour - mass diagram for the rest frame colour  $(u - r)_{\text{res}}$  and the intrinsic colour  $(u - r)_{\text{int}}$  differ significantly in each redshift bin. With the introduction of the extinction correction, a significant part of the galaxies from the green valley passes into the blue cloud. This is due to the fact that a significant part of the green valley galaxies is obscured star-forming galaxies (30–65 per cent; Díaz-García et al. 2019), the proportion of which depends on the redshift and stellar mass. The proportion of such galaxies in the near Universe is not large, but it is not negligible (Schawinski et al. 2014). At high redshifts, the proportion of dusty green valley galaxies increases even more.

### 6.3 Identification of blue and red galaxies

We use the technique of dividing galaxies into a red sequence and a blue cloud, developed in the (Díaz-García et al. 2019) for galaxies from the ALHAMBRA survey in the redshift range from  $0.1 \leq z \leq 1.1$ . The ALHAMBRA survey used a set of 20 mid-band filters in the optical range, as well as near-infrared filters J, H, and K<sub>S</sub>. Using the SED-fitting method, the authors determined the physical properties

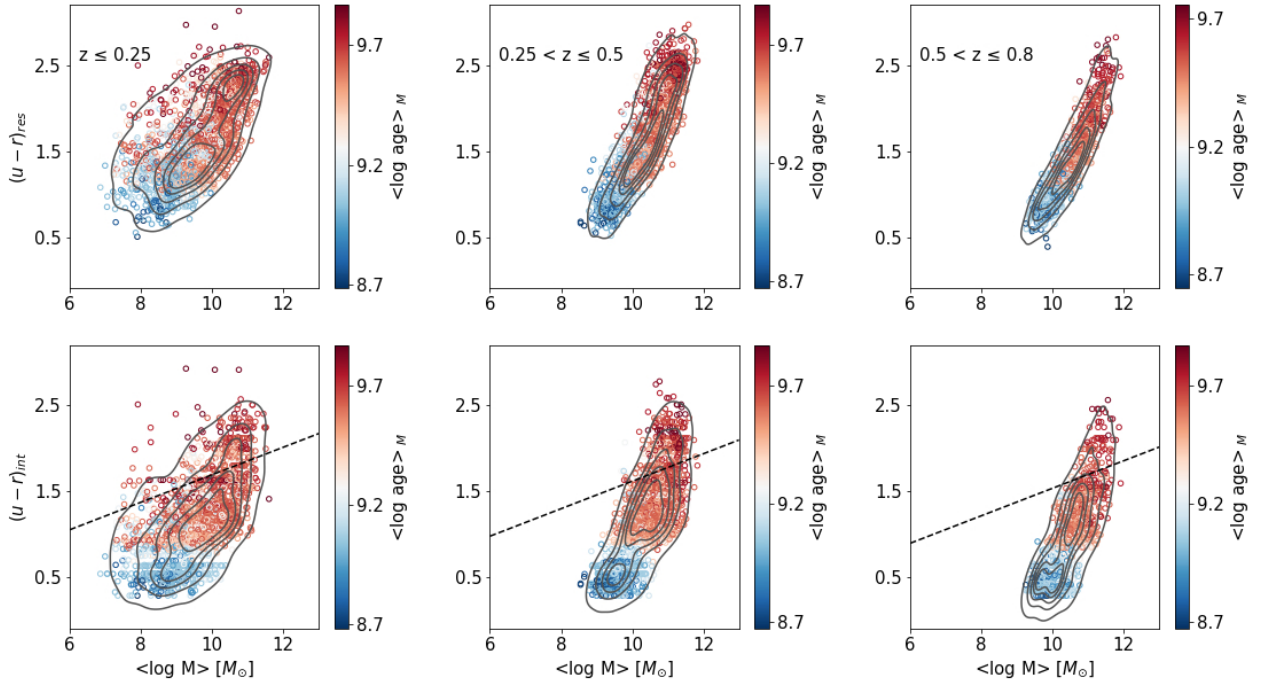


**Figure 13.** Colour-mass relation for rest frame (top panels) and intrinsic (bottom panels) colour ( $u - r$ ) in the three redshift bins:  $z \leq 0.25$ ,  $0.25 < z \leq 0.5$ , and  $0.5 < z \leq 0.8$  (from left to right). The dashed line shows the limiting intrinsic colour for galaxy classification for the mean redshift in each bin (see more details in the Section 6.3).

of galaxy populations, such as stellar mass, rest-frame colour, and extinction of each galaxy. This allowed them to divide the galaxies from the sample into a red sequence and a blue cloud. They found the proportion of dusty star-forming galaxies in the green valley using intrinsic colours and contamination in the samples of rest frame galaxies, determined using classical colour diagrams, caused by the obscuring of star-forming galaxies. The authors concluded that the use of a mass - colour diagram can reduce the contamination of a part of the galaxies from the red sequence by 20 per cent compared with the use of colour - colour diagrams.

In the (Díaz-García et al. 2019, eq.3), the equation defining the limit of the separation of galaxies into a red sequence and a blue cloud used the true colours for the  $m_{F365}$  and  $m_{F551}$  filters. In (González Delgado et al. 2021, eq.5), this criterion was recalculated into colours  $(u - r)_{\text{int}}$  that similar to our photometric system. So we can use this equation 2 without any corrections.

$$(u - r)_{\text{res}}^{\lim} = 0.16 \cdot (\log M - 10.0) - 0.3 \cdot (z - 0.1) + 1.7, \quad (1)$$

where  $z$  is the photometric redshift of each galaxy and  $\log M$  is its stellar mass.

Galaxies from gMOSS survey are labeled as quiescent if intrinsic colour is redder than the limiting value  $(u - r)_{\text{res}}^{\lim}$  else galaxies are star-forming.

#### 6.4 Characterization of blue and red galaxies

Using the criterion for selecting star-forming and quiet galaxies from equation 2, we obtained that about  $\sim 86$  per cent of the sample from our survey are blue cloud galaxies, and the share of red sequence galaxies accounts for the remaining  $\sim 14$  per cent. Figure 14 shows the distribution of the fractions of the red sequence and blue cloud galaxies from a complete sample with threshold magnitude  $r_{AB} = 22.5$  mag up to the redshift  $z = 0.8$ . Figure 14 shows a general trend towards a decrease in the proportion of quiescent galaxies from  $\sim 14$  per cent for  $z \leq 0.1$  to  $\sim 8$  per cent for  $0.7 \leq z < 0.8$  and increases in the proportion of star-forming galaxies through redshift from  $\sim 86$  per cent for  $z \leq 0.1$  to  $\sim 92$  per cent for  $0.7 \leq z < 0.8$ , respectively.

Figure 15 shows distributions of properties of stellar populations for two separate galaxy populations for the rest frame  $(u - r)_{\text{res}}$  colour, total stellar mass, extinction  $A_V$ . In common red galaxies have a redder colour  $(u - r)_{\text{int}}$  and lower extinction. Also, galaxies from the red sequence are more massive.

The separation of galaxies into two groups using the colour - mass diagram can be justified either by differences in the evolutionary path of the galaxy or by differences in stellar content. Next, we will discuss the dependence of the properties of stellar populations of galaxies on redshift.

In Figure 16, we investigate the evolution of the intrinsic colour, stellar mass, and age of galaxies through redshift. We obtain average estimates of these characteristics of galaxies for each bin by redshift. Red and blue galaxies are distributed on these diagrams according to their stellar component.

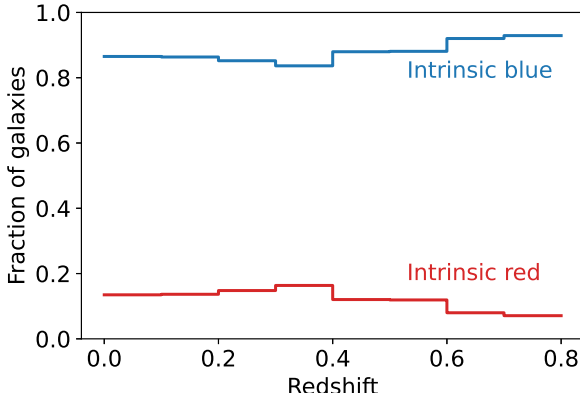


**Figure 14.** The fraction of red sequence and blue cloud galaxies obtained by  $(u - r)_{\text{res}}^{\lim}$  criteria through the redshift with bin  $z = 0.1$

The  $(u - r)_{\text{int}}$  colour distribution shows that both red and blue galaxies become bluer at high redshifts. For red galaxies, the first redshift bin shows a slightly bluer  $(u - r)_{\text{int}}$  colour than on intermediate redshifts.

On average, blue galaxies are about 0.8 dex lighter than red ones. At the same time, a significant decrease in this difference is observed for the galaxy of the near Universe ( $z \leq 0.1$ ), this may be due to a shift caused by the fact that faint galaxies become invisible with an increase in redshift. In addition, the fact that the average mass in each of the galaxy populations increases with the growth of the redshift should be associated with the same reason.

The galaxies of the red sequence and the blue cloud are quite well separated in the diagram showing the stellar age. At any redshift, red galaxies are older by  $\sim 0.35$  dex. This is probably a consequence of different histories of star formation (SFH) and/or the formation of blue and red galaxies. The age of both blue and red galaxies decreases with increasing redshift, indicating ongoing star formation and/or reflecting a biased sample for low-mass galaxies at higher redshifts.

## 6.5 Star formation rate density

The most prominent result in the study of the evolution of galaxies through the redshift is that it has been established that the star formation rate density has a peak at  $z \sim 3$  and is decreasing until present cosmic time (Lilly et al. 1996; Madau et al. 1998; Hopkins & Beacom 2006; Fardal et al. 2007; Gunawardhana et al. 2013; Madau & Dickinson 2014; Driver et al. 2018).

In order to study the star formation rate density (SFRD), it is necessary to study the incompleteness of our sample and the limits of detection of the stellar mass depending on the redshift. It is necessary to find the minimum and maximum redshifts ( $z_{\min}$  and  $z_{\max}$ ) at which each galaxy of the sample can be detected due to the detection limits of cMOSS. The sample consists of galaxies in the range from 15.1 to 22.5 mag in  $r$  SDSS filter, which we used as constraints. In order to estimate the maximum and minimum redshifts, we used the limits for detecting stellar magnitudes in cMOSS sample and the properties of the stellar population obtained using the CIGALE code. The average values of  $z_{\min}$  and  $z_{\max}$  were obtained in bins by the stellar mass with a width of  $\Delta \log(M) = 0.2$  dex.

Figure 17 shows the result of our estimates of the detection limit by stellar mass as a function of the redshift. Galaxies with a mass

of  $\log(M)_{[\text{M}_\odot]} \sim 10$  dex can be detected in the entire redshift range ( $z \leq 0.8$ ) presented in the sample. Low-mass galaxies of  $\log(M)_{[\text{M}_\odot]} \sim 8.0$  can be detected up to  $z = 0.15$ . Also Figure 17 show that we are able to study samples of galaxies with stellar masses above  $\log(M)_{[\text{M}_\odot]} \sim 8.9, 9.5$ , and  $9.9$  dex at  $z = 0.4, 0.6$ , and  $0.8$ , respectively.

Thus, our results allow us to study the SFRD for galaxies in the redshift range  $z \leq 0.15$  using the star formation history (SFH) for galaxies in the gMOSS sample obtained by the CIGALE code. At the upper limit of the redshift range ( $z = 0.15$ ), the sample of galaxies includes galaxies with a mass above  $10^8 \text{ M}_\odot$ . Galaxies with a mass below this limit have made a significant contribution to the history of star formation over the past 4 Gyr. In the cMOSS galaxy sample, such galaxies are detected in the range up to  $z = 0.15$ , however, their number is insufficient to assess the incompleteness of the sample.

To obtain SFRD, taking into account the effect of the incompleteness of volume, we divided the star-formation rate (SFR) of each galaxy at  $0.005 \leq z \leq 0.15$  by its maximum comoving volume ( $V_{\max}$ ). Since only a small number of galaxies with a mass below  $10^8 \text{ M}_\odot$  are not observed at  $z = 0.15$  ( $\sim 3$  per cent), we can assume that  $V_{\max}$  is equal to the comoving volume  $V_c$  at this redshift range:

$$V_{\max} = \Delta V = V_c(z = 0.15) - V_c(z = 0.005). \quad (2)$$

The SFRs were obtained from the parametric delayed SFH with optional exponential burs for a 1 Gyr resampling. The error of  $\log \rho$  in each epoch is obtained by propagating the SFRD dispersion in each bin. The results shown in Figure 18 demonstrate that  $\log \rho$  increases with redshift, up to  $z \sim 3.0$  and then begins to decrease.

We compared the results obtained with those already known in the literature in the works (Panter et al. 2007; Madau & Dickinson 2014; Driver et al. 2018; López Fernández et al. 2018; Sánchez et al. 2019; Leja et al. 2019; Bellstedt et al. 2020; González Delgado et al. 2021). These results are obtained from different data samples and using different analysis techniques. Overall, we conclude that the analysis of gMOSS sample provides results that are in good agreement with cosmological surveys (Madau & Dickinson 2014; Driver et al. 2018) as well as the nearby galaxies analysis f SDSS (Panter et al. 2007), IFS CALIFA (López Fernández et al. 2018), and GAMA (Bellstedt et al. 2020).

## 7 CONCLUSIONS

We have presented gMOSS, a new medium-band photometric catalogue that covers  $2.386 \text{ deg}^2$  of the HS47.5-22 field, which includes measurements of 16 medium-band and 4 broadband filters of the SDSS system (we publish general fluxes and corresponding uncertainties of  $1\sigma$ ), and photometric redshifts of 19,875 galaxies. The sample of galaxies in the gMOSS survey is limited by threshold magnitude  $r_{\text{AB}} = 22.5$  mag. Also, we present the spectral redshifts obtained from observations at the 6-meter Russian telescope with SCORPIO-2 multi-mode focus reducer for selected galaxies in the HS47.5-22 field.

We applied the SED-fitting code CIGALE to extract the star formation history of 12,281 galaxies up to  $z = 0.8$ . We used a set of spectral evolution synthesis models from the BC03 set Bruzual & Charlot (2003), with the modified attenuation law by Calzetti et al. (2000) and assuming the initial mass function of Chabrier (2003). We have obtained the stellar mass, rest frame and internal  $(u - r)$  colours, extinction, age and metallicity of galaxy stellar populations. The standard deviations in the stellar population parameters are:

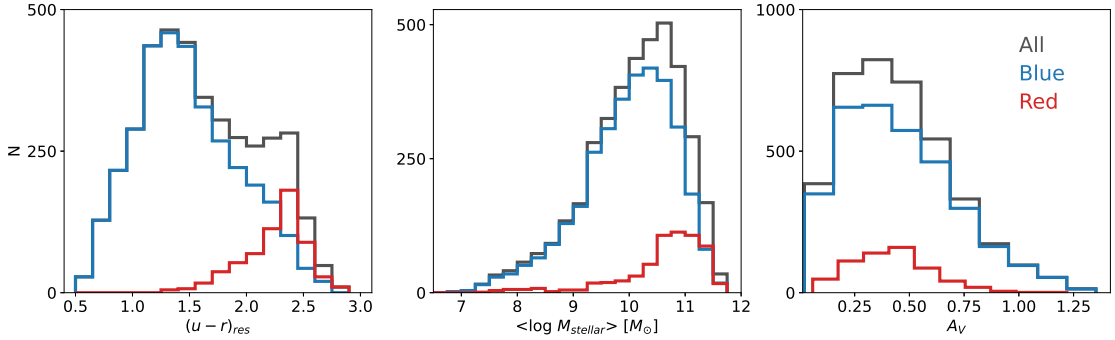


**Figure 15.** Distributions of properties of stellar populations for two separate galaxy populations for the rest frame ( $u-r$ ) colour, total stellar mass, extinction  $A_V$ . The complete sample is indicated by a black line, the galaxies of the red sequence are red, the blue clouds are blue.

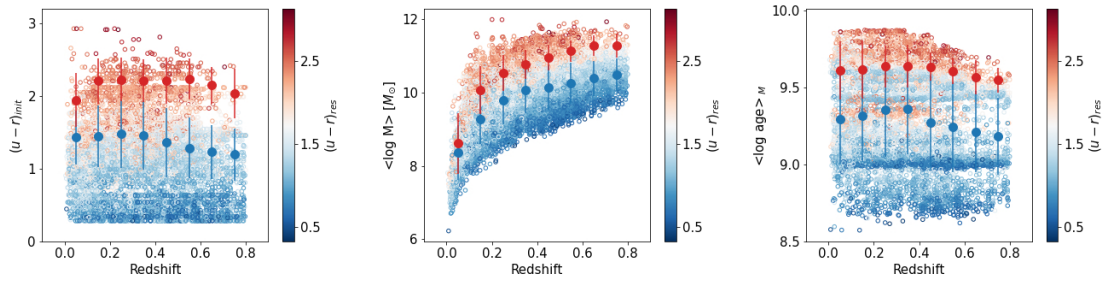


**Figure 16.** Evolution of the intrinsic colour, stellar mass, and age of galaxies. Dots represent the average values of each property in each redshift bin. The dispersion with respect to the average values is shown as error bars. Blue and red dots correspond to the blue cloud and red sequence galaxies, respectively.

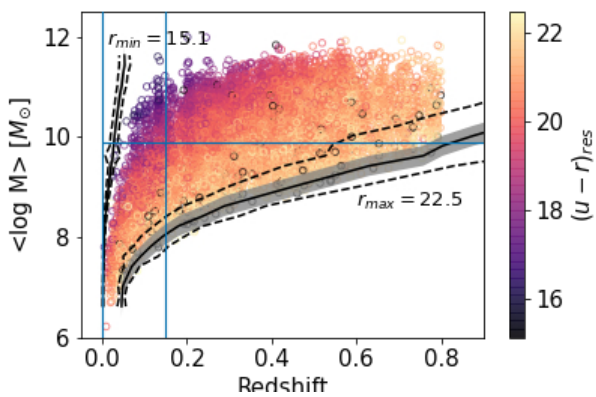


**Figure 17.** Distribution of redshifts and stellar masses obtained by CIGALE for each of the galaxies in the sample. The black lines show the  $z_{\max}$  and  $z_{\min}$  values that correspond to the limiting magnitudes from 15.1 to 22.5 mag of the cMOSS galaxy survey. The shaded regions illustrate the dispersion of limiting magnitude in the y-axis, and the dashed lines the dispersion in the x-axis. The blue lines show the sub-sample of galaxies with  $z \leq 0.15$  used to explore the evolution of the star formation rate density. Colour bar code galaxy magnitudes in the  $r$  SDSS band.

$0.19 \pm 0.08$  mag,  $0.12 \pm 0.05$  dex,  $0.10 \pm 0.04$  dex, and  $0.28 \pm 0.09$  mag for  $(u-r)_{\text{res}}$  colour, total stellar mass, mass-weighted age, and

extinction, respectively. For the metallicity parameter, we used a set of 6 discrete values, so this parameter is less amenable to analysis.

We have divided the galaxies into blue and red populations. The easiest way to split a full galaxy sample is to use the dust-corrected  $(u-r)_{\text{int}}$  diagram. The percentage of the number of the red sequence galaxies and the blue cloud galaxies is 14 per cent and 86 per cent, respectively. The properties of stellar populations clearly differ between red sequence and blue cloud galaxies. Red and blue galaxies are identified by their  $(u-r)_{\text{int}}$  colour, with mean values  $\sim 2$  and  $\sim 1$ . Throughout the full redshift range ( $0 < z \leq 0.8$ ), red galaxies are older and more massive than blue ones.

The evolution of galaxies with redshift shows that at the present cosmic time galaxies are older than at  $z = 0.8$ . The average mass of galaxies increases with increasing redshift, which is a manifestation of the selection of a flux-limited sample.

As part of the study of the star formation rate density, we determined that our sample is complete for galaxies with above  $<\log M> [M_\odot] \sim 8.9, 9.5$ , and  $9.9$  dex at  $z = 0.4, 0.6$ , and  $0.8$ , respectively. Based on the obtained SFRD data at  $z \sim 0.1$ , we can estimate the evolution of SFRD, obtaining a result that corresponds to the results of previously published works of cosmological surveys.

## ACKNOWLEDGEMENTS

The work was carried out within the framework of the government contract of SAO RAS approved by the Ministry of Science and

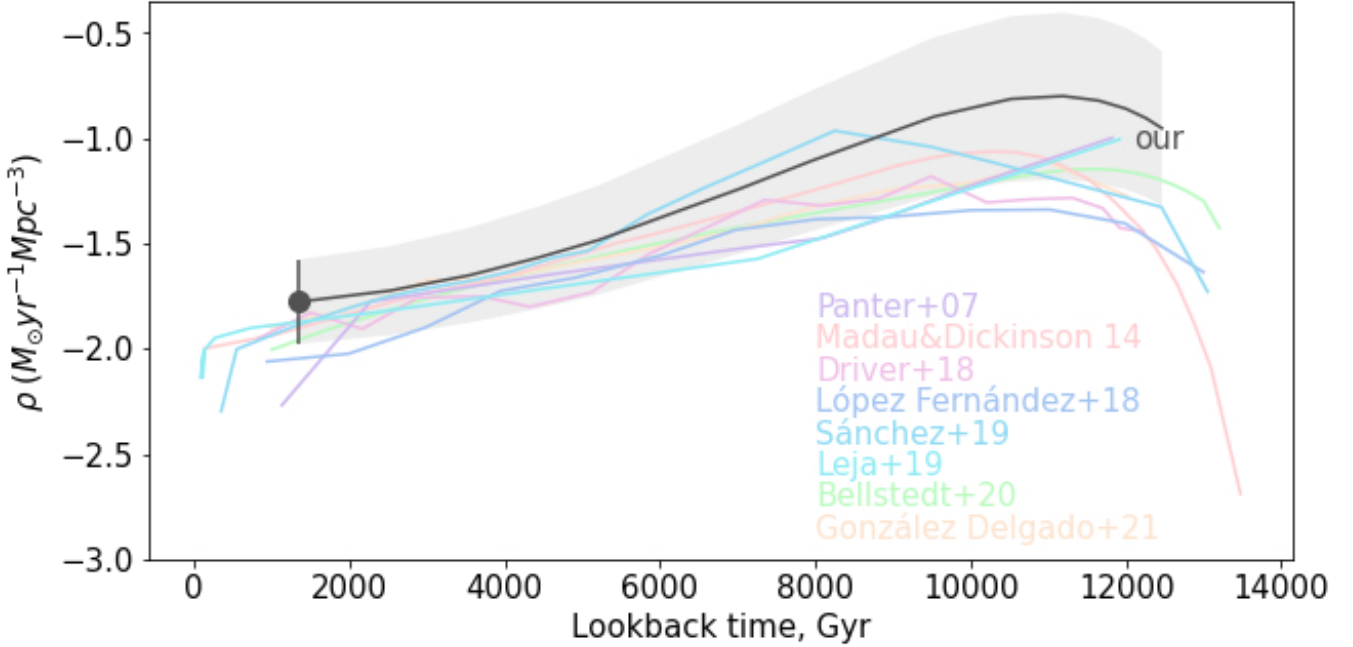


**Figure 18.** SFRD evolution through cosmic time obtained from the SED-fitting results (gray line) with the nearby galaxies ( $0.05 \leq z \leq 0.15$ , gray dot). Grey shadow area represents the uncertainties of the result. The different colour lines show the SFRDs obtained in other works.

Higher Education of the Russian Federation. Observations with the SAO RAS telescopes are supported by the Ministry of Science and Higher Education of the Russian Federation (including agreement No05.619.21.0016, project ID RFMEFI61919X0016).

This research has made use of the NASA/IPAC Extragalactic Database (NED), which is operated by the Jet Propulsion Laboratory, California Institute of Technology, under contract with the National Aeronautics and Space Administration.

Funding for the Sloan Digital Sky Survey IV has been provided by the Alfred P. Sloan Foundation, the U.S. Department of Energy Office of Science, and the Participating Institutions. SDSS-IV acknowledges support and resources from the Center for High-Performance Computing at the University of Utah. The SDSS web site is [www.sdss.org](http://www.sdss.org).

This work has made use of data from the European Space Agency (ESA) mission *Gaia* (<https://www.cosmos.esa.int/gaia>), processed by the *Gaia* Data Processing and Analysis Consortium (DPAC, <https://www.cosmos.esa.int/web/gaia/dpac/consortium>). Funding for the DPAC has been provided by national institutions, in particular the institutions participating in the *Gaia* Multilateral Agreement.

The Legacy Surveys consist of three individual and complementary projects: the Dark Energy Camera Legacy Survey (DECaLS; Proposal ID #2014B-0404; PIs: David Schlegel and Arjun Dey), the Beijing-Arizona Sky Survey (BASS; NOAO Prop. ID #2015A-0801; PIs: Zhou Xu and Xiaohui Fan), and the Mayall z-band Legacy Survey (MzLS; Prop. ID #2016A-0453; PI: Arjun Dey). DECaLS, BASS and MzLS together include data obtained, respectively, at the Blanco telescope, Cerro Tololo Inter-American Observatory, NSF's NOIRLab; the Bok telescope, Steward Observatory, University of Arizona; and the Mayall telescope, Kitt Peak National Observatory, NOIRLab. The Legacy Surveys project is honored to be permitted to conduct

astronomical research on Iolkam Du'ag (Kitt Peak), a mountain with particular significance to the Tohono O'odham Nation.

NOIRLab is operated by the Association of Universities for Research in Astronomy (AURA) under a cooperative agreement with the National Science Foundation.

This project used data obtained with the Dark Energy Camera (DECam), which was constructed by the Dark Energy Survey (DES) collaboration. Funding for the DES Projects has been provided by the U.S. Department of Energy, the U.S. National Science Foundation, the Ministry of Science and Education of Spain, the Science and Technology Facilities Council of the United Kingdom, the Higher Education Funding Council for England, the National Center for Supercomputing Applications at the University of Illinois at Urbana-Champaign, the Kavli Institute of Cosmological Physics at the University of Chicago, Center for Cosmology and Astro-Particle Physics at the Ohio State University, the Mitchell Institute for Fundamental Physics and Astronomy at Texas A & M University, Financiadora de Estudos e Projetos, Fundacao Carlos Chagas Filho de Amparo, Financiadora de Estudos e Projetos, Fundacao Carlos Chagas Filho de Amparo a Pesquisa do Estado do Rio de Janeiro, Conselho Nacional de Desenvolvimento Cientifico e Tecnologico and the Ministerio da Ciencia, Tecnologia e Inovacao, the Deutsche Forschungsgemeinschaft and the Collaborating Institutions in the Dark Energy Survey. The Collaborating Institutions are Argonne National Laboratory, the University of California at Santa Cruz, the University of Cambridge, Centro de Investigaciones Energeticas, Medioambientales y Tecnologicas-Madrid, the University of Chicago, University College London, the DES-Brazil Consortium, the University of Edinburgh, the Eidgenossische Technische Hochschule (ETH) Zurich, Fermi National Accelerator Laboratory, the University of Illinois at Urbana-Champaign, the Institut de Ciencias de l'Espai (IEEC/CSIC), the Institut de Fisica d'Altes Energies, Lawrence Berkeley National Laboratory, the Ludwig Maximilians Universitat Munchen and the

associated Excellence Cluster Universe, the University of Michigan, NSF's NOIRLab, the University of Nottingham, the Ohio State University, the University of Pennsylvania, the University of Portsmouth, SLAC National Accelerator Laboratory, Stanford University, the University of Sussex, and Texas A&M University.

BASS is a key project of the Telescope Access Program (TAP), which has been funded by the National Astronomical Observatories of China, the Chinese Academy of Sciences (the Strategic Priority Research Program “The Emergence of Cosmological Structures” Grant # XDB09000000), and the Special Fund for Astronomy from the Ministry of Finance. The BASS is also supported by the External Cooperation Program of Chinese Academy of Sciences (Grant # 114A11KYSB20160057), and Chinese National Natural Science Foundation (Grant # 11433005).

The Legacy Survey team makes use of data products from the Near-Earth Object Wide-field Infrared Survey Explorer (NEOWISE), which is a project of the Jet Propulsion Laboratory/California Institute of Technology. NEOWISE is funded by the National Aeronautics and Space Administration.

The Legacy Surveys imaging of the DESI footprint is supported by the Director, Office of Science, Office of High Energy Physics of the U.S. Department of Energy under Contract No. DE-AC02-05CH1123, by the National Energy Research Scientific Computing Center, a DOE Office of Science User Facility under the same contract; and by the U.S. National Science Foundation, Division of Astronomical Sciences under Contract No. AST-0950945 to NOAO.

## DATA AVAILABILITY

All data is available to the reviewer(s) on <https://github.com/alegro/gMOSS> and will be made open-source on publication.

## REFERENCES

- Afanasiev V. L., Moiseev A. V., 2011, *Baltic Astronomy*, **20**, 363
- Ahumada R., et al., 2020, *ApJS*, **249**, 3
- Bellstedt S., et al., 2020, *MNRAS*, **498**, 5581
- Benítez N., et al., 2009, *ApJ*, **691**, 241
- Benítez N., et al., 2014, arXiv e-prints, p. arXiv:1403.5237
- Bertin E., Arnouts S., 1996, *Astronomy and Astrophysics Supplement*, **117**, 393
- Boquien M., Burgarella D., Roehlly Y., Buat V., Ciesla L., Corre D., Inoue A. K., Salas H., 2019, *A&A*, **622**, A103
- Bruzual G., Charlot S., 2003, *MNRAS*, **344**, 1000
- Burgarella D., Buat V., Iglesias-Páramo J., 2005, *MNRAS*, **360**, 1413
- Calzetti D., Armus L., Bohlin R. C., Kinney A. L., Koornneef J., Storchi-Bergmann T., 2000, *ApJ*, **533**, 682
- Capak P., et al., 2004, *AJ*, **127**, 180
- Carnall A. C., McLure R. J., Dunlop J. S., Davé R., 2018, *MNRAS*, **480**, 4379
- Chabrier G., 2003, *PASP*, **115**, 763
- Chevallard J., Charlot S., 2016, *MNRAS*, **462**, 1415
- Coil A. L., Hennawi J. F., Newman J. A., Cooper M. C., Davis M., 2007, *The Astrophysical Journal*, **654**, 115
- Colless M., et al., 2003, arXiv e-prints, pp astro-ph/0306581
- Cooper M. C., et al., 2006, *Monthly Notices of the Royal Astronomical Society*, **370**, 198
- Dey A., et al., 2019, *AJ*, **157**, 168
- Díaz-García L. A., et al., 2019, *A&A*, **631**, A156
- Dodonov S. N., Chilingarian I. V., 2008, *Astrophysical Bulletin*, **63**, 1
- Dodonov S. N., Kotov S. S., Movsesyan T. A., Gevorkyan M., 2017, *Astrophysical Bulletin*, **72**, 473
- Draine B. T., et al., 2014, *ApJ*, **780**, 172
- Driver S. P., et al., 2018, *MNRAS*, **475**, 2891
- Fardal M. A., Katz N., Weinberg D. H., Davé R., 2007, *MNRAS*, **379**, 985
- Feldmann R., et al., 2006, *Monthly Notices of the Royal Astronomical Society*, **372**, 565
- Gaia Collaboration et al., 2016, *A&A*, **595**, A1
- Gaia Collaboration et al., 2018, *A&A*, **616**, A1
- Gerke B. F., et al., 2005, *The Astrophysical Journal*, **625**, 6
- González Delgado R. M., et al., 2014, *A&A*, **562**, A47
- González Delgado R. M., et al., 2021, arXiv e-prints, p. arXiv:2102.13121
- Gunawardhana M. L. P., et al., 2013, *MNRAS*, **433**, 2764
- Han Y., Han Z., 2012, *ApJ*, **749**, 123
- Han Y., Han Z., 2014, *ApJS*, **215**, 2
- Han Y., Han Z., 2019, *ApJS*, **240**, 3
- Hopkins A. M., Beacom J. F., 2006, *ApJ*, **651**, 142
- Johnson B. D., Leja J., Conroy C., Speagle J. S., 2020, *bd-j/prospector*: prospector v1.0.0, doi:10.5281/zenodo.4586953
- Kashikawa N., et al., 2004, *PASJ*, **56**, 1011
- Kauffmann G., et al., 2003, *MNRAS*, **341**, 54
- Le Fèvre O., et al., 2005, *Astronomy and Astrophysics*, **439**, 877
- Leja J., Johnson B. D., Conroy C., van Dokkum P. G., Byler N., 2017, *The Astrophysical Journal*, **837**, 170
- Leja J., Carnall A. C., Johnson B. D., Conroy C., Speagle J. S., 2019, *ApJ*, **876**, 3
- Lilly S. J., Le Fevre O., Hammer F., Crampton D., 1996, *ApJ*, **460**, L1
- Lilly S. J., et al., 2007, *The Astrophysical Journal Supplement Series*, **172**, 70
- Lockman F. J., Jahoda K., McCammon D., 1986, *ApJ*, **302**, 432
- López Fernández R., et al., 2018, *A&A*, **615**, A27
- Madau P., Dickinson M., 2014, *ARA&A*, **52**, 415
- Madau P., Pozzetti L., Dickinson M., 1998, *ApJ*, **498**, 106
- Malmquist K. G., 1922, *Meddelanden från Lunds Astronomiska Observatorium Serie I*, **100**, 1
- Meneux B., et al., 2006, *Astronomy and Astrophysics*, **452**, 387
- Moles M., et al., 2008, *Astronomical Journal*, **136**, 1325
- Molthagen K., Wendker H. J., Briel U. G., 1997, *Astronomy & Astrophysics Supplement series*, **126**, 509
- Moresco M., et al., 2013, *A&A*, **558**, A61
- Murayama T., et al., 2007, *The Astrophysical Journal Supplement Series*, **172**, 523
- Noll S., Burgarella D., Giovannoli E., Buat V., Marcillac D., Muñoz-Mateos J. C., 2009, *A&A*, **507**, 1793
- Oke J. B., Gunn J. E., 1983, *ApJ*, **266**, 713
- Panter B., Jimenez R., Heavens A. F., Charlot S., 2007, *MNRAS*, **378**, 1550
- Peng Y. J., et al., 2010, *Astrophysical Journal*, **721**, 193
- Planck Collaboration et al., 2018, *A&A*, **617**, A48
- Robotham A. S. G., Bellstedt S., Lagos C. d. P., Thorne J. E., Davies L. J., Driver S. P., Bravo M., 2020, *MNRAS*, **495**, 905
- Sánchez S. F., et al., 2019, *MNRAS*, **482**, 1557
- Schawinski K., et al., 2014, *MNRAS*, **440**, 889
- Wolf C., et al., 2004, *Astronomy and Astrophysics*, **421**, 913
- Yasuda N., et al., 2001, *AJ*, **122**, 1104
- da Cunha E., Charlot S., Elbaz D., 2008, *MNRAS*, **388**, 1595

This paper has been typeset from a *TeX/LaTeX* file prepared by the author.